Research Article | Vol. 26, No. 9 | 30 Apr 2018 | OPTICS EXPRESS 11147

Optics EXPRESS

Aluminum nitride integrated photonics platform for the ultraviolet to visible spectrum

TSUNG-JU LU,[1,6,*] MICHAEL FANTO,[2,3,6] HYEONGRAK CHOI,[1] PAUL THOMAS,[2] JEFFREY STEIDLE,[2] SARA MOURADIAN,[1] WEI KONG,[4] DI ZHU,[1] HYOWON MOON,[1] KARL BERGGREN,[1] JEEHWAN KIM,[4] MOHAMMAD SOLTANI,[5] STEFAN PREBLE,[2] AND DIRK ENGLUND[1]

[1]*Department of Electrical Engineering and Computer Science, Massachusetts Institute of Technology, Cambridge, Massachusetts 02139, USA*
[2]*Microsystems Engineering, Rochester Institute of Technology, Rochester, New York 14623, USA*
[3]*Air Force Research Laboratory, Rome, New York 13441, USA*
[4]*Department of Mechanical Engineering, Massachusetts Institute of Technology, Cambridge, Massachusetts 02139, USA*
[5]*Raytheon BBN Technologies, Cambridge, Massachusetts 02138, USA*
[6]*These authors contributed equally to this work*
[*]*tsungjul@mit.edu*

Abstract: We demonstrate a wide-bandgap semiconductor photonics platform based on nanocrystalline aluminum nitride (AlN) on sapphire. This photonics platform guides light at low loss from the ultraviolet (UV) to the visible spectrum. We measure ring resonators with intrinsic quality factor (Q) exceeding 170,000 at 638 nm and Q >20,000 down to 369.5 nm, which shows a promising path for low-loss integrated photonics in UV and visible spectrum. This platform opens up new possibilities in integrated quantum optics with trapped ions or atom-like color centers in solids, as well as classical applications including nonlinear optics and on-chip UV-spectroscopy.

© 2018 Optical Society of America under the terms of the OSA Open Access Publishing Agreement

OCIS codes: (130.2790) Guided waves; (130.3120) Integrated optics devices; (140.4780) Optical resonators; (050.2770) Gratings.

References and links

1. R. Krischek, W. Wieczorek, A. Ozawa, N. Kiesel, P. Michelberger, T. Udem, and H. Weinfurter, "Ultraviolet enhancement cavity for ultrafast nonlinear optics and high-rate multiphoton entanglement experiments," Nat. Photonics **4** (3), 170–173 (2010).
2. M. Soltani, R. Soref, T. Palacios, and D. Englund, "AlGaN/AlN integrated photonics platform for the ultraviolet and visible spectral range," Opt. Express **24**, 25415 (2016).
3. K. Nemoto, M. Trupke, S. J. Devitt, A. M. Stephens, B. Scharfenberger, K. Buczak, T. Nöbauer, M. S. Everitt, J. Schmiedmayer, and W. J. Munro, "Photonic Architecture for Scalable Quantum Information Processing in Diamond," Phys. Rev. X **4** (3), 031022 (2014).
4. M. Pant, H. Choi, S. Guha, and D. Englund, "Percolation based architecture for cluster state quantum computation using photon-mediated entanglement between atomic memories," https://arXiv:1704.07292 (2017).
5. L.-M. Duan and C. Monroe, "*Colloquium*: quantum networks with trapped ions," Rev. Mod. Phys. **82**, 1209–1224 (2010).
6. E. Togan, Y. Chu, A. S. Trifonov, L. Jiang, J. Maze, L. Childress, M. V. G. Dutt, A. S. Sørensen, P. R. Hemmer, A. S. Zibrov, and M. D. Lukin, "Quantum entanglement between an optical photon and a solid-state spin qubit," Nature **466** (7307), 730–734 (2010).
7. L. Childress, R. Walsworth, and M. Lukin, "Atom-like crystal defects: From quantum computers to biological sensors," Phys. Today **67** (10), 38–43 (2014).
8. C. Xiong, W. H. P. Pernice, X. Sun, C. Schuck, K. Y. Fong, and H. X. Tang, "Aluminum nitride as a new material for chip-scale optomechanics and nonlinear optics," New J. Phys. **14**, 095014 (2012).
9. K. K. Mehta, C. D. Bruzewicz, R. McConnell, R. J. Ram, J. M. Sage, and J. Chiaverini, "Integrated optical addressing of an ion qubit," Nat. Nanotechnol. **11**, 1066 (2016).
10. S. L. Mouradian, T. Schröder, C. B. Poitras, L. Li, J. Goldstein, E. H. Chen, M. Walsh, J. Cardenas, M. L. Markham, D. J. Twitchen, M. Lipson, and D. Englund, "Scalable integration of long-lived quantum memories into a photonic circuit," Phys. Rev. X **5**, 031009 (2015).

#318428 https://doi.org/10.1364/OE.26.011147
Journal © 2018 Received 26 Feb 2018; revised 2 Apr 2018; accepted 3 Apr 2018; published 16 Apr 2018

11. C. Xiong, W. H. P. Pernice, and H. X. Tang, "Low-loss, Silicon Integrated, Aluminum Nitride Photonic Circuits and Their Use for Electro-Optic Signal Processing," Nano Lett. **12** (7), 3562–3568 (2012).
12. C. Xiong, X. Sun, K. Y. Fong, and H. X. Tang, "Integrated high frequency aluminum nitride optomechanical resonators," Appl. Phys. Lett. **100**, 171111 (2012).
13. S. P. Fang and H. F. Taylor, "High-performance single-mode fiber-optic switch," Opt. Lett. **19**, 1204–1206 (1994).
14. W. H. P. Pernice, C. Xiong, C. Schuck, and H. X. Tang, "Second harmonic generation in phase matched aluminum nitride waveguides and micro-ring resonators," Appl. Phys. Lett. **100** (22), 223501 (2012).
15. Y. Fujii, S. Yoshida, S. Misawa, S. Maekawa, and T. Sakudo, "Nonlinear optical susceptibilities of AlN film," Appl. Phys. Lett. **31**, 815-816 (1977).
16. H. Jung, C. Xiong, K. Y. Fong, X. Zhang, and H. X. Tang, "Optical frequency comb generation from aluminum nitride microring resonator," Opt. Lett. **38**, 2810–2813 (2013).
17. H. Jung, R. Stoll, X. Guo, D. Fischer, and H. X. Tang, "Green, red, and IR frequency comb line generation from single IR pump in AlN microring resonator," Optica **1**, 396 (2014).
18. X. Guo, C.-L. Zou, H. Jung, and H. X. Tang, "On-Chip Strong Coupling and Efficient Frequency Conversion between Telecom and Visible Optical Modes," Phys. Rev. Lett. **117** (12), 123902 (2016).
19. X. Liu, C. Sun, B. Xiong, L. Wang, J. Wang, Y. Han, Z. Hao, H. Li, Y. Luo, J. Yan, T. Wei, Y. Zhang, and J. Wang, "Integrated continuous-wave aluminum nitride Raman laser," Optica **4**, 893–896 (2017).
20. T. Troha, M. Rigler, D. Alden, I. Bryan, W. Guo, R. Kirste, S. Mita, M. D. Gerhold, R. Collazo, Z. Sitar, and M. Zgonik, "UV second harmonic generation in AlN waveguides with modal phase matching," Opt. Mater. Express **6** (6), 2014–2023 (2016).
21. H. Jung and H. X. Tang, "Aluminum nitride as nonlinear optical material for on-chip frequency comb generation and frequency conversion," Nanophotonics **5** (2), 263–271 (2016).
22. X. Guo, C.-L. Zou, C. Schuck, H. Jung, R. Cheng, and H. X. Tang, "Parametric down-conversion photon-pair source on a nanophotonic chip," Light Sci. Appl. **6** (5), e16249 (2017).
23. X. Liu, C. Sun, B. Xiong, L. Wang, J. Wang, Y. Han, Z. Hao, H. Li, Y. Luo, J. Yan, T. Wei, Y. Zhang, and J. Wang, "Broadband frequency comb generation in aluminum nitride-on-sapphire microresonators," https://arXiv:1611.01994v2 (2016).
24. P. T. Lin, H. Jung, L. C. Kimerling, A. Agarwal, and H. X. Tang, "Low-loss aluminium nitride thin film for mid-infrared microphotonics," Laser Photon. Rev. **8**, L23–L28 (2014).
25. A. Patra, R. E. Tallman, and B. A. Weinstein, "Effect of crystal structure and dopant concentration on the luminescence of Cr^{3+} in Al_2O_3 nanocrystals," Opt. Mater. **27**, 1396–1401 (2005).
26. I. Parkhomenko, L. Vlasukova, F. Komarov, O. Milchanin, M. Makhavikou, A. Mudryi, V. Zhivulko, J. Żuk, P. Kopyciński, D. Murzalinov, "Origin of visible photoluminescence from Si-rich and N-rich silicon nitride films," Thin Solid Films **626**, 70–75 (2017).
27. C. Monroe and J. Kim, "Scaling the ion trap quantum processor," Science **339**, 1164–1169 (2013).
28. A. Goban, C.-L. Hung, S.-P. Yu, J. D. Hood, J. A. Muniz, J. H. Lee, M. J. Martin, A. C. McClung, K. S. Choi, D. E. Chang, O. Painter, and H. J. Kimble, "Atom-light interactions in photonic crystals," Nat. Commun. **5**, 3808 (2014).
29. J. K. W. Yang and K. K. Berggren, "Using high-contrast salty development of hydrogen silsesquioxane for sub-10-nm half-pitch lithography," J. Vac. Sci. Technol. B **25** (6), 2025 (2007).
30. A. Yariv, "Critical coupling and its control in optical waveguide-ring resonator systems," IEEE Photonics Technology Letters **14**, 483–485 (2002).
31. A. Yariv, "Universal relations for coupling of optical power between microresonators and dielectric waveguides," Electronics Letters **36**, 321–322 (2000).
32. J. Levy, "Integrated nonlinear optics in silicon nitride waveguides and resonators," PhD Thesis (2011).
33. A. Dutt, "On-chip Quantum and Nonlinear Optics: From Squeezing to Spectroscopy," PhD Thesis (2017).
34. S. A. Miller, M. Yu, X. Ji, A. G. Griffith, J. Cardenas, A. L. Gaeta, and M. Lipson, "Low-loss silicon platform for broadband mid-infrared photonics," Optica **4**, 707–712 (2017).
35. J. Mower, N. C. Harris, G. R. Steinbrecher, Y. Lahini, and D. Englund, "High-fidelity quantum state evolution in imperfect photonic integrated circuits," Phys. Rev. A **92**, 032322 (2015).
36. J. C. Mikkelsen, W. D. Sacher, and J. K. S. Poon, "Dimensional variation tolerant silicon-on-insulator directional couplers," Opt. Express **22**, 3145–3150 (2014).
37. M. Stegmaier, J. Ebert, J. M. Meckbach, K. Ilin, M. Siegel, and W. H. P. Pernice, "Aluminum nitride nanophotonic circuits operating at ultraviolet wavelengths," Appl. Phys. Lett. **104**, 091108 (2014).
38. X. Liu, C. Sun, B. Xiong, L. Wang, J. Wang, Y. Han, Z. Hao, H. Li, Y. Luo, J. Yan, T. Wei, Y. Zhang, and J. Wang, "Aluminum nitride-on-sapphire platform for integrated high-Q microresonators," Opt. Express **25**, 587–594 (2017).
39. A. Gorin, A. Jaouad, E. Grondin, V. Aimez, and P. Charette, "Fabrication of silicon nitride waveguides for visible-light using PECVD: a study of the effect of plasma frequency on optical properties," Opt. Express **16**, 13509–13516 (2008).
40. L. Hoffman, A. Subramanian, P. Helin, B. Du Bois, R. Baets, P. Van Dorpe, G. Gielen, R. Puers, and D. Braeken, "Low Loss CMOS-Compatible PECVD Silicon Nitride Waveguides and Grating Couplers for Blue Light Optogenetic Applications," IEEE Photon. J. **8** (5), 2701211 (2016).
41. D. Y. Oh, K. Y. Yang, C. Fredrick, G. Ycas, S. A. Diddams, and K. J. Vahala, "Coherent ultra-violet to near-infrared generation in silica ridge waveguides," Nat. Commun. **8**, 13922 (2017).

42. H. Lee, T. Chen, J. Li, O. Painter, and K. J. Vahala, "Ultra-low-loss optical delay line on a silicon chip," Nat. Commun. **3**, 1–7 (2012).
43. M. J. R. Heck, J. F. Bauters, M. L. Davenport, D. T. Spencer, and J. E. Bowers, "Ultra-low loss waveguide platform and its integration with silicon photonics," Laser Photonics Rev. **8** (5), 667–686 (2014).
44. G. Poberaj, R. Degl'Innocenti, C. Medrano, and P. Günter, "UV integrated optics devices based on beta-barium borate," Optical Materials **31**, 1049–1053 (2009).
45. J. Schroeder, R. Mohr, C. J. Montrose, and P. B. Macedo, "Light Scattering in a Number of Optical Grade Glasses," J. Non-Cryst. Solids **40**, 313–320 (1980).
46. B. Aspar, H. Moriceau, E. Jalaguier, C. Lagahe, A. Soubie, B. Biasse, A. M. Papon, A. Claverie, J. Grisolia, G. Benassayag, F. Letertre, O. Rayssac, T. Barge, C. Maleville, and B. Ghyselen, "The Generic Nature of the Smart-Cut® Process for Thin Film Transfer," J. Electron. Mater. **30**, 834–840 (2001).
47. H. Miyake, C. H. Lin, K. Tokoro, and K. Hiramatsu, "Preparation of high-quality AlN on sapphire by high-temperature face-to-face annealing," J. Cryst. Growth **456**, 155–159 (2016).
48. B. Karunagaran, S. J. Chung, S. Velumani, and E.-K. Suh, "Effect of rapid thermal annealing on the properties of PECVD SiN_x thin films," Mater. Chem. Phys. **106**, 130–133 (2007).
49. M. Feneberg, R. A. R. Leute, B. Neuschl, K. Thonke, and M. Bickermann, "High-excitation and high-resolution photoluminescence spectra of bulk AlN," Phys. Rev. B **82**, 075208 (2010).
50. R. H. French, "Electronic Band Structure of Al_2O_3, with Comparison to Alon and AIN," J. Am. Ceram. Soc. **73** (3), 477–489 (1990).
51. A. Majkić, U. Puc, A. Franke, R. Kirste, R. Collazo, Z. Sitar, and M. Zgonik, "Optical properties of aluminum nitride single crystals in the THz region," Opt. Mater. Express **5**, 2106 (2015).
52. A. Majkić, U. Puc, A. Franke, R. Kirste, R. Schlesser, R. Collazo, Z. Sitar, and M. Zgonik, "Optical nonlinear and electro-optical coefficients in bulk aluminium nitride single crystals," Phys. Status Solidi B **254**, 1700077 (2017).
53. D. J. Moss, R. Morandotti, A. L. Gaeta, and M. Lipson, "New CMOS-compatible platforms based on silicon nitride and Hydex for nonlinear optics," Nat. Photonics **7**, 597–607 (2013).
54. J. S. Levy, A. Gondarenko, M. A. Foster, A. C. Turner-Foster, A. L. Gaeta, and M. Lipson, "CMOS-compatible multiple wavelength oscillator for on-chip optical interconnects," Nat. Photonics **4** (1), 37–40 (2010).
55. D. Néel, I. Roland, X. Checoury, M. El Kurdi, S. Sauvage, P. Boucaud, C. Brimont, T. Guillet, B. Gayral, and F. Semond, "AlN photonic crystals and microdisks for UV nanophotonics," Adv. Nat. Sci: Nanosci. Nanotechnol. **5**, 023001 (2014).
56. J. Sellés, C. Brimont, G. Cassabois, P. Valvin, T. Guillet, I. Roland, Y. Zeng, X. Checoury, P. Boucaud, M. Mexis, F. Semond, and B. Gayral, "Deep-UV nitride-on-silicon microdisk lasers," Sci. Rep. **6**, 21650 (2016).
57. G. Piazza, P. J. Stephanou, and A. P. Pisano, "Piezoelectric aluminum nitride vibrating contour-mode MEMS resonators," J. Microelectromech. Syst. **15** (6), 1406–1418 (2006).
58. C. M. Lueng, H. L. W. Chan, C. Surya, and C. L. Choy, "Piezoelectric coefficient of aluminum nitride and gallium nitride," J. Appl. Phys. **88**, 5360–5363 (2000).
59. S. Miller, Y.-H. D. Lee, J. Cardenas, A. L. Gaeta, and M. Lipson, "Electro-optic effect in silicon nitride," in Proceedings of CLEO (2015), paper SF1G.4.
60. A. Z. Subramanian, P. Neutens, A. Dhakal, R. Jansen, T. Claes, X. Rottenberg, F. Peyskens, S. Selvaraja, P. Helin, B. Du Bois, K. Leyssens, S. Severi, P. Deshpande, R. Baets, and P. Van Dorpe, "Low-loss singlemode PECVD silicon nitride photonic wire waveguides for 532-900 nm wavelength window fabricated within a CMOS pilot line," IEEE Photon. J. **5** (6), 2202809 (2013).
61. P. Muellner, A. Maese-Novo, E. Melnik, R. Hainberger, G. Koppitsch, J. Kraft, and G. Meinhardt, "CMOS-compatible low-loss silicon nitride waveguide integration platform for interferometric sensing," in Proceedings of ECIO (2016).
62. K. Ikeda, R. E. Saperstein, N. Alic, and Y. Fainman, "Thermal and Kerr nonlinear properties of plasma-deposited silicon nitride/ silicon dioxide waveguides," Opt. Express **16** (17), 12987–12994 (2008).

1. Introduction

Aluminum nitride (AlN) is one of the widest bandgap (6.015 eV, ~205 nm) semiconductors with attractive electronic and photonic properties, including transparency into the ultraviolet (UV) regime (365 nm wavelength and shorter). This broad spectrum makes it attractive for applications including UV spectroscopy [1, 2], optical waveguides for modular quantum computing with atomic memories [3–7], nonlinear photonics throughout the UV to infrared [8], and solar-blind communications [2]. Many atomic transitions are in the UV or visible (VIS) spectrum, including Ytterbium ions ($^{171}Yb^+$), Strontium ions ($^{88}Sr^+$), Barium ions ($^{138}Ba^+$), and nitrogen vacancy (NV) centers in diamond, which have important optical transitions at 369.5 nm, 422 nm, 650 nm, and 637 nm, respectively. Recent work demonstrates the utility of integrated optics to perform quantum coherent operations on the optical qubit transition of $^{88}Sr^+$ at 647 nm [9]; the UV transmission of AlN-on-sapphire would also enable $^{88}Sr^+$ initialization at 422 nm or driving the

Optics EXPRESS

369.5 nm wavelength of $^{171}Yb^+$. Autofluorescence of silicon nitride (SiN) presents a challenge for pumping the diamond NV center at 532 nm [10]; this autofluorescence is greatly reduced in AlN-on-sapphire, opening the path to large-scale photonic integrated circuits for atom-like qubits in diamond.

Electro-optic modulation presents an important capability in many applications, such as architectures for modular quantum computing. AlN has a relatively large electro-optic coefficient, and fast electro-optic modulation (~4.5 Gb/s) has been demonstrated with AlN's high c-axis electro-optic coefficient (r_{33} = 1 pm/V) using sputtered AlN [11]. Piezo-electric actuation of photonic devices has also been shown with optomechanical resonators [12] and can potentially achieve very high modulation depth [13]. Lastly, AlN has a high second order nonlinear susceptibility $\chi^{(2)}$ (4.7 pm/V) [14, 15], as well as a third order nonlinear susceptibility with Kerr coefficient comparable to that of stoichiometric SiN (the n_2 for transverse electric waveguide mode in the (001) plane is estimated to be $(2.3 \pm 1.5) \times 10^{-15}$ cm^2/W) [16]. These nonlinear properties allow for a number of nonlinear optical processes [17–19], including second harmonic generation [14, 20], sum/difference frequency generation [21], photon pair generation by spontaneous parametric down conversion [22], and four-wave mixing [16, 23]. The combination of the large bandgap with these nonlinear and electro-optic properties make AlN a promising platform for quantum devices and for other high-performance optics applications.

Here, we present a UV/VIS photonics platform based on AlN grown by plasma vapor deposition of nanocolumns on a sapphire substrate. X-ray diffraction shows low defect densities, which will help minimize propagation loss. We demonstrate essential photonic devices including ring resonators, distributed Bragg reflectors, and directional couplers. We show ring resonators with high intrinsic quality factor (Q) in visible (Q ~ 170k, loss ~ 5.3 dB/cm at 638 nm) and record-high quality factor in UV (Q ~ 20k, loss ~ 75 dB/cm at 369.5 nm). We demonstrate both vertical and edge coupling and compare them with simulation results. While autofluorescence is a problem in materials such as SiN, we find it to be low in the AlN on sapphire platform.

2. Material

Figure 1(a) illustrates the commercially available AlN-on-Sapphire wafers from Kyma Technologies, Inc., consisting of 430 μm sapphire (Al_2O_3) with a 200 ± 10 nm c-plane AlN film on the top layer, which is used for fabricating photonic integrated circuits (PICs) in this work. The c-plane AlN is grown on top of the sapphire substrate by pulsed DC magnetron sputtering, using a process called plasma vapor deposition of nanocolumns (PVDNC). This method produces an AlN thin film that is crystalline with the [0001] direction parallel to the growth direction. Atomic force microscopy of the AlN thin film shown in the inset of Fig. 1(a) indicates a flat surface with 0.9 nm RMS roughness. High-resolution X-ray diffraction (HRXRD) measurements in Fig. 1(b) indicate the high structural quality of the AlN thin film. The ω scan of (002) and (015) AlN peaks shows full-width-half-maximum (FWHM) of 0.12 degree and 0.20 degree respectively, while previous work of AlN thin films deposited on amorphous silica reported a FWHM of the XRD rocking curve to be less than 2 degrees with a 1 degree FWHM resolution limit in their system [24]. The single crystalline wurtzite structure across the wafer is evidenced by the (015) ϕ scan showing six-fold symmetry [Fig. 1(c)]. This flat surface and improved structural quality likely contribute to the low waveguide loss described below. Figure 1(d) plots the measured refractive index of the AlN film spanning from UV to VIS to near infrared wavelengths.

Figure 1(e) shows the power dependence of this platform's background autofluorescence using a scanning confocal microscope with a λ = 532 nm excitation pump laser (Coherent Verdi). A 0.95 numerical aperture (NA) microscope objective (Olympus UMPlanFl 100x) is used for the scanning confocal microscope, and a 532 nm notch filter as well as a 550 nm long-pass filter are used to filter out the 532 nm excitation pump in the fluorescence collection path. The photoluminescence (PL) is then fiber-coupled from free-space to a single-mode fiber via a 0.4 NA

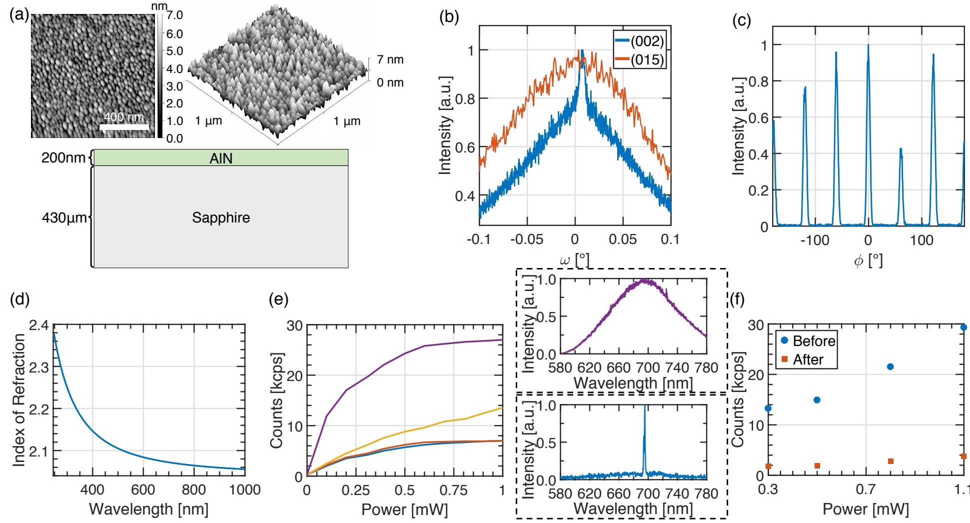

Fig. 1. Properties of AlN-on-sapphire material. (a) Cross section illustrating each layer of the wafer, along with their respective thickness; top inset: atomic force microscopy scan of AlN film showing the nanocolumn size. Surface roughness is measured to be 0.9 nm RMS with 26.5 nm grain size (b) High resolution x-ray diffraction (002) and (015) ω scan of AlN. (c) (015) ϕ scan of AlN showing six-fold symmetry wurtzite structure. (d) Refractive index measurements using ellipsometry. (e) Background fluorescence from sapphire substrate (yellow), unpatterned AlN (blue), patterned AlN (orange), and stoichiometric silicon nitride (purple). Top inset (purple): Fluorescence spectrum of SiN. Bottom inset (blue): Fluorescence spectrum of AlN. (f) Background fluorescence from SiON top cladding, before (blue circles) and after (orange squares) bleaching.

microscope objective (Olympus MA 20). The fiber-collected PL signal is either detected using single-photon avalanche photodiodes (Excelitas) or spectrally resolved on a grating spectrometer (Princeton Instruments, Acton SP2500i). We are using the 4 µm diameter fiber facet as the pinhole for confocal imaging. Since the size of this fiber facet is not matched perfectly to the spot size at the sample plane, we collect a portion of the out-of-focus light. As such, when we measure the AlN autofluorescence, we are also pumping the underlying sapphire that is out-of-focus and collecting a portion of the sapphire PL. This claim is supported by the fluorescence spectrum of the AlN, which is shown in the bottom inset spectrum of Fig. 1(e). The AlN fluorescence spectrum is identical to that of the sapphire (not shown), which is in agreement with the fluorescence spectrum of sapphire found in literature [25]. The narrow luminescence double peaks at around 695 nm correspond to the ruby luminescence from the $^2E \rightarrow 4A_2$ transitions of Cr^{3+} ions that are substitutional in the Al sublattice.

For comparison, Fig. 1(e) also shows the autofluorescence results of a SiN sample under the same excitation and collection conditions; the fluorescence spectrum of SiN is also shown in the top inset of Fig. 1(e). The SiN sample has close to four times the amount of fluorescence intensity as AlN; however, the amount of autofluorescence is dependent on the SiN composition and method of deposition [26]. Furthermore, the PL from pumping the AlN is mainly from the underlying sapphire substrate. Spectrally, this sapphire fluorescence is concentrated in a narrow band sapphire Cr line at around 695 nm, which can be easily filtered out by a notch filter. This is more favorable for quantum applications compared to the broadband SiN PL from 620 nm to 780 nm, which overlaps spectrally to NV in diamond spectrum [10]. A low autofluorescence makes AlN promising for interfacing with atomic transitions of ions [27], neutral atoms [28],

and atom-like defects in diamond [10]. Ultimately the maximum allowed background count highly depends on the applications and protocol of the experiment. As long as the background fluorescence is optically detuned from the optical transitions of the quantum system one is working with, sufficient filtering can be achieved to improve signal-to-noise ratio.

Initially after deposition, the SiON cladding (to be discussed later) exhibits some fluorescence comparable to SiN, but we found that the SiON fluorescence can be bleached away by optically pumping the material with the excitation laser, as shown in Fig. 1(f). This photobleaching method of the SiON top cladding did not have any effect on the AlN or SiN materials.

3. Fabrication

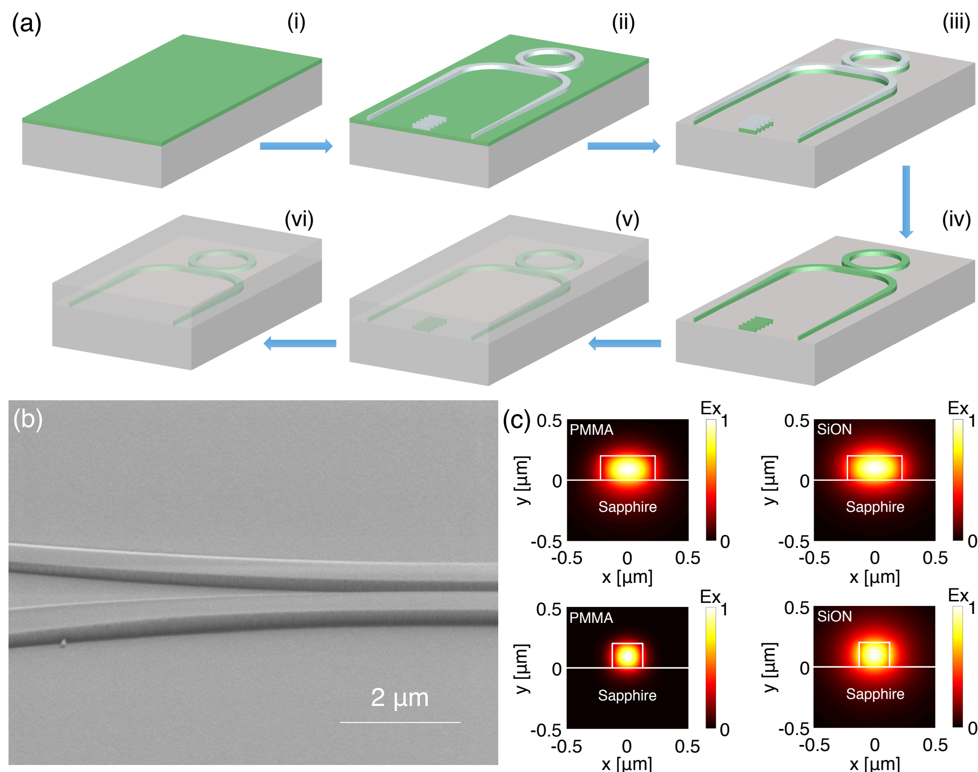

Fig. 2. (a) AlN on sapphire photonics fabrication process: (i) Start off with an unpatterned AlN-on-sapphire chip diced up from a whole wafer. (ii) Spin coat HSQ (2% XR-1541), pattern using electron beam lithography, and develop using an aqueous mixture of 1 wt % NaOH and 4 wt % NaCl for high contrast. (iii) Etch by ICP-RIE using chlorine chemistry. (iv) Strip HSQ. (v) Clad with silicon oxynitride using plasma-enhanced chemical vapor deposition (PECVD). (vi) Edge polish for making the inverse-tapered edge couplers. (b) Scanning electron microscope (SEM) image of a fabricated AlN waveguide at a 50 degrees tilted view. (c) Transversal component of TE mode in AlN waveguide for PMMA and SiON cladding for 638 nm (top) and 400 nm (bottom) wavelengths. The dimensions of the waveguide for 638 nm wavelength are 450 nm wide × 200 nm thick. The dimensions of the waveguide for 400 nm wavelength are 250 nm wide × 200 nm thick.

Figures 3, 4, and 5 demonstrate the various essential optical components, designed for top-cladding with either (i) Poly(methyl methacrylate) (PMMA), which has a refractive index of $n_{PMMA} \approx 1.50$ to 1.49 in the wavelength range of 500 nm to 700 nm, or (ii) silicon oxynitride

Optics EXPRESS

SiO_xN_y (SiON), with a refractive index matched to the underlying sapphire ($n_{sapphire} \approx 1.76$ to 1.75 in the wavelength range of 360 nm to 480 nm) by adjusting the composition of oxygen and nitrogen to achieve a refractive index between that of silica (1.45) and silicon nitride (2.1). The PMMA cladding is used for the devices and measurements in the VIS wavelength range of 500 nm to 700 nm, while the SION cladding is used for the devices and measurements in the UV wavelength range of 360 nm to 480 nm.

Figure 2(a) outlines the complete fabrication process. The process starts off with an unpatterned 1 cm × 1 cm AlN-on-sapphire chip diced from a whole wafer. Then, hydrogen silsesquioxane (2% XR-1541) is spun on after deposition of a 5 nm thick Cr discharge layer via electron beam evaporation. The hydrogen silsesquioxane (HSQ) film thickness is measured to be ~70 nm by using an AFM to measure the step feature profile after patterning. The patterns are written with an Elionix ELS-F125 electron beam lithography system at 125 kV. The patterns are developed using a salty developer, which is an aqueous mixture of 1 wt % NaOH and 4 wt % NaCl, for high contrast [29]. The AlN waveguides and photonic components are etched at an etch rate of 200 nm/min by inductively coupled plasma reactive-ion etching (ICP-RIE) using a gas mixture of $BCl_3/Cl_2/Ar$. We do not observe a significant change in the surface roughness from the etching, and a sidewall angle close to 90 degrees is achieved due to the combination of physical sputtering and plasma chemical etching. The $BCl_3/Cl_2/Ar$ chemistry ICP-RIE etch does not result in any noticeable etching of the underlying sapphire substrate. Hence, the underlying sapphire acts as an etch stop layer in which we can overetch the AlN to ensure that it is completely cleared through without creating a sapphire ridge underneath the AlN waveguide structures. The Cr and HSQ are lastly removed with Cr etchant and buffered oxide etch (BOE), respectively. Figure 2(b) shows a scanning electron microscope (SEM) image of the fabricated AlN waveguide. Finally, the waveguides are clad with approximately 3 microns of SION using plasma-enhanced chemical vapor deposition (PECVD) or spin coated with approximately 2 microns of PMMA. In the case where the chip is cladded with SiON, the edges of the chip are mechanically polished back to the inverse-tapered waveguides for edge coupling.

4. Chip design and components

4.1. Coupling methods

Figure 3 highlights two methods to couple light into and from the PIC: grating couplers and inverse-tapered edge couplers. Due to the narrow frequency response of grating couplers, two different grating couplers are used for testing components in the visible wavelength from 500 nm to 700 nm wavelength: a green wavelength grating coupler optimized for 500 nm to 600 nm [shown in the top SEM image of Fig. 3(a)] and a red wavelength grating coupler optimized for 600 nm to 700 nm [shown in the bottom SEM image of Fig. 3(a)]. Figures 3(b) and 3(c) show comparisons between the simulated coupling efficiency spectra and the experimentally measured transmission spectra for the green and red wavelength grating couplers, respectively. The general shape of the experimental grating coupler transmission spectra matches well with the simulated coupling efficiency spectra. The experimental coupling efficiencies are listed in arbitrary units because we do not experimentally mode-match the spatial modes of the grating coupler and collection objective. The peak experimental transmission intensity for the green wavelength grating coupler is 0.1544 [a.u.] at 532.9 nm, while the peak experimental transmission intensity for the red wavelength grating coupler is 0.1565 [a.u.] at 625.3 nm.

Both green and red wavelength grating couplers are optimized for TE polarization, so the simulated coupling efficiencies model the collection of TE polarized light injected into the 450 nm wide by 200 nm tall AlN waveguide on bulk sapphire and scattered by the grating coupler. For the green wavelength grating coupler, the first gap width is 60 nm and the first grating period is 285 nm. Then, the gap width and grating period both linearly increase from 101 nm and 325 nm to 150 nm and 346 nm, respectively (increasing linearly in each period for 17 periods). Finally,

Optics EXPRESS

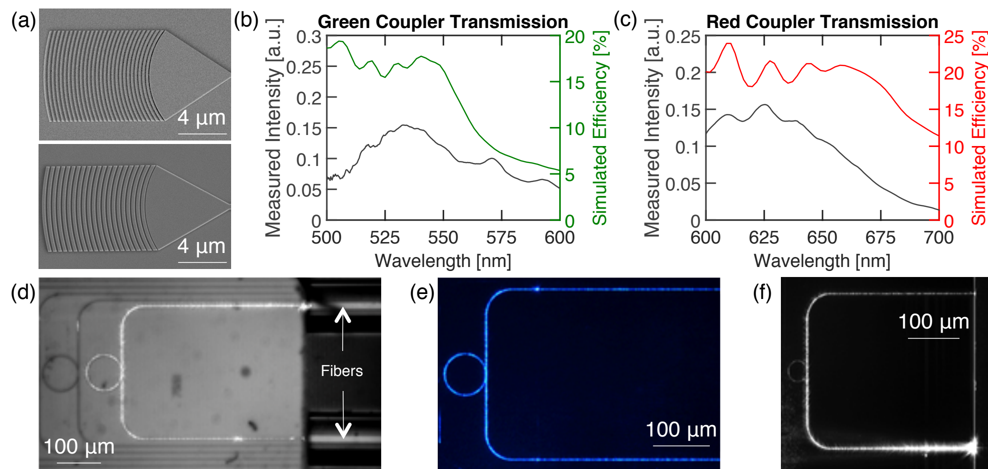

Fig. 3. (a) SEM images of the grating couplers. First gap of the grating coupler is 60 nm, and the gaps are linearly increasing. Curvatures are set to be matched with mode evolution so that there is no reflection. Top: green spectrum grating coupler. Bottom: red spectrum grating coupler (b) Green line: simulated coupling efficiency vs. wavelength plot of green-spectrum grating coupler optimized for 500 to 600 nm. Black line: measured experimental transmission intensity vs. wavelength plot of green-spectrum grating coupler. (c) Red line: simulated coupling efficiency vs. wavelength plot of red-spectrum grating coupler optimized for 600 to 700 nm. Black line: measured experimental transmission intensity vs. wavelength plot of red-spectrum grating coupler. (d) Fiber edge coupling to the waveguides at 369.5 nm using Nufern SM300 fiber. (e), (f) Free-space edge coupling using aspheric lenses into a waveguides that are designed to be single mode in the traverse electric polarization at 468 nm and 369.5 nm, respectively.

the gratings maintain a gap width of 150 nm and grating period of 346 nm for the remaining 9 periods. In a similar fashion, for the red wavelength grating coupler, the first gap width is 60 nm and the first grating period is 285 nm. Then, the gap width and grating period both linearly increase from 101 nm and 401 nm to 132 nm and 414 nm, respectively (increasing in each period for 10 periods). Finally, the gratings maintain a gap width of 132 nm and grating period of 414 nm for the remaining 10 periods. For both the green and red wavelength grating couplers, the dimensions of each individual grating periods are optimized in order for the spatial mode profile of the diffracted light to be a Gaussian field profile. The grating couplers are also designed to be cladded with PMMA, rather than simple air cladding, in order to increase the out-of-plane coupling efficiency by pulling more of the optical mode away from the underlying sapphire substrate as PMMA has a higher refractive index than air. Both grating couplers are designed for an etch depth of 200 nm in order for ease of fabrication so that the grating couplers and waveguides can be fabricated in the same steps with no additional processing. Therefore, we believe grating couplers with even higher collection efficiency can be achieved with partially etched gratings. All measurements done in the VIS wavelength range of 500 nm to 700 nm use grating couplers for coupling light into and out of the chip.

Next, the fiber edge coupling is shown in Fig. 3(d), with UV fiber (Nufern SM300) and an excitation wavelength of 369.5 nm. Figures 3(e) and 3(f) show free-space edge coupling using aspheric lenses into waveguides that are designed to be single mode in the traverse electric polarization at 468 and 369.5 nm, respectively. The inverse-tapered waveguides adiabatically transform and expand the AlN waveguide mode to the fiber waveguide mode at the chip's edge facet. As such, for the inverse-tapered edge couplers, a SiON cladding is used in order for the

refractive indices of the materials surrounding the AlN waveguide to be to be uniform such that the AlN waveguide mode can be expanded in a circularly symmetric way in order to match to the Gaussian mode of a fiber at the chip's edge facet. All measurements done in the UV wavelength range of 360 nm to 480 nm use edge couplers for coupling light into and out of the chip. It is difficult to quantify the experimental edge coupling loss based on the sources of loss we have. In measuring the transmission loss of sending light into the input edge coupler facet and collecting from the output edge coupler facet, the light propagates along a waveguide that spans across multiple electron beam lithography write fields. At each write field boundary, a dislocation of the waveguide due to stitching errors result in scattering points that contribute to the overall facet-to-facet transmission loss. As such, measuring the transmission loss is not an accurate estimation for the edge coupler coupling loss. However, we are able to achieve at least 40% transmission from input edge facet to output edge facet in our devices.

4.2. Ring resonators

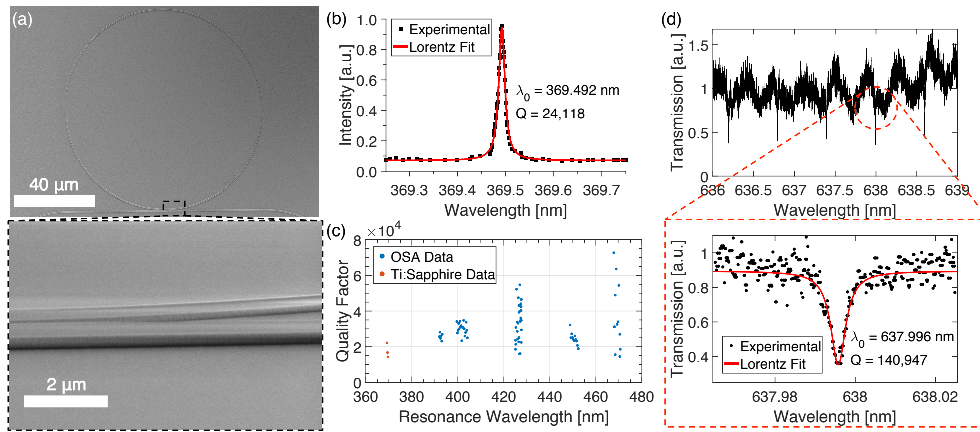

Fig. 4. (a) SEM of the ring resonator. Inset shows a close up of the ring resonator at a 50 degrees tilted view. The gap between the waveguide and the ring is 300 nm for the undercoupling regime, which was used to verify the unloaded Q. (b) Wavelength response at 369.5 nm of the ring resonator cladded with SiON around resonance. The Lorentzian fitting shows a Q of >24,000. (c) Quality factors of 40 µm radius ring resonators measured using an optical spectrum analyzer (OSA) for wavelengths spanning from 380 nm to 480 nm, along with the quality factors at 369.5 nm wavelength using both frequency doubled pulsed and continuous-wave (CW) TI:Sapphire lasers. (d) Wavelength response at 637 nm of the ring resonator cladded with PMMA around resonance. The Lorentzian fitting shows a Q of >140,000. Inset shows a zoom-in of the wavelength response.

Figure 2(c) shows simulated electric field profiles of the AlN waveguide modes for PMMA and SiON cladding for 400 nm and 638 nm wavelengths. The waveguides support a single transverse electric (TE) mode for their respective wavelengths. Wrapping these waveguides into rings produces the high Q resonators. The ring resonator measurements are summarized in Fig. 4. Figure 4(b) shows the response at 369.5 nm of the 40 µm radius ring resonator cladded with SiON around resonance; a Lorentzian fit indicates a Q of >24,000. The resonance in the ring is measured by mapping the intensity of the light scattering from the ring by means of a UV sensitive camera placed in a microscope above the device. After measuring several devices with increasingly larger waveguide-ring gaps and finding the coupling of the waveguide to the ring decreases each time without transitioning from overcoupled regime to critically coupled regime to undercoupled regime (or at least just from the critically coupled regime to undercoupled regime), we find the

smallest waveguide-ring gap resonator to be undercoupled. Since the resonator is undercoupled, the ring resonance cannot be measured directly through an access bus waveguide. Hence, the data shows a resonance peak rather than a dip. Figure 4(c) shows the quality factors of various 40 μm radius ring resonators measured using an optical spectrum analyzer (OSA) for various sampled resonance wavelengths spanning from 380 nm to 480 nm, along with the quality factors at around 369.5 nm using both a frequency doubled pulsed Ti:Sapphire laser (Spectra-Physics Mai Tai) and a continuous-wave (CW) tunable Ti:Sapphire laser (M Squared SolsTiS). The spacings between the sets of sampled wavelengths are not indicative of the ring resonator's Free-Spectral-Range (FSR). Rather, the Free-Spectral-Ranges of the various 40 μm radius ring resonators that we measure from 360 nm to 480 nm span from 0.22 nm to 0.4 nm. If we assume that the propagation loss is dominated by the sidewall scattering loss and linear absorption loss of the material, then we can estimate the propagation loss using the following equation for calculating the loss rate α given the resonator Q, where n_g is the group index [30–34]:

$$Q = \frac{2\pi n_g}{\lambda\alpha} \tag{1}$$

Then, the loss can be calculated by:

$$\text{loss} = 10\log_{10}\left(e^{-\alpha}\right) \tag{2}$$

To calculate the loss in units of dB/cm, λ in Eq. (1) should be in units of cm. Thus, the Q of >24,000 at 369.5 nm wavelength corresponds to a propagation loss of 75 dB/cm, where we measure the n_g to be 2.45 experimentally from the FSR of the ring by the equation:

$$n_g = \frac{\lambda^2}{(\text{FSR})(L)} \tag{3}$$

where L is the length of one round trip around the closed cavity.

Figure 4(d) shows the frequency response of a 50 μm radius ring resonator cladded with PMMA around resonance in the red wavelength range. We probe the 50 μm radius ring with an evanescently coupled access waveguide. The Lorentzian fitting shows a loaded Q of >140,000 at 638 nm, and we measure the n_g to be 2.15 experimentally from the FSR of the 50 μm radius ring. In order to obtain the intrinsic Q of the ring resonator, we can use the following [30–34]:

$$Q_i = \frac{2Q_l}{1 \pm \sqrt{T_0}} \tag{4}$$

where Q_i is the intrinsic Q, Q_l is the loaded Q, T_0 is the normalized transmitted power at the resonance wavelength, and the + and − signs correspond to under- and over-coupled regimes, respectively. Since the ring resonator is operating in the undercoupled regime, we find the intrinsic Q to be >170,000, which corresponds to a propagation loss of 5.3 dB/cm.

These ring resonators are useful for measuring the waveguide propagation loss (in the undercoupled regime). In the critically coupled regime, or in a drop-port configuration, they serve as on-chip filters as needed for filtering atomic fluorescence, for example [10]. They can also be used for on-chip photon pair generation [22].

In terms of ring resonator performance, the PMMA cladding should be better than SiON since the PMMA can flow into the gap between the ring resonator and bus waveguide in order to completely fill that up. By nature of PECVD deposition, the SiON cannot completely fill in the gap between the ring resonator and bus waveguide. However, the SiON is necessary for making edge couplers with high coupling efficiency and mode matching to a fiber, so SiON is used for cladding the ring resonators with resonance at around 369.5 nm. Furthermore, since PMMA is a polymer, it is not suitable for UV wavelengths due to autofluorescence.

4.3. Distributed Bragg reflector

Distributed Bragg reflectors (DBRs) represent another important PIC component as broadband on-chip reflectors and filters. To further support this point, we develop a distributed Bragg reflector with high extinction for 532 nm for use as on-chip filtering of the excitation pump light used for exciting NV centers in diamond. The DBR has a period of 140 nm with 50% duty cycle, and it is designed to have an adiabatic tapering from the regular waveguide into the DBR in order to have low insertion loss. Also, the DBR is designed to structurally have rounded features for ease of fabrication. Figure 5(a) shows an SEM image of the fabricated DBR. The overlay blue plot in Fig. 5(b) shows the simulated transmission spectrum for the DBR, which has 45 dB extinction for the 532 nm green pump light. The black plot in Fig. 5(b) shows at least 13 dB extinction experimentally for the DBR. We expect the extinction to be even higher because the attenuated 532 nm signal was at the noise floor of our experimental system.

The decreased transmission of the DBR simulation at wavelengths around 500 nm is due to the third order TE mode at around 500 nm wavelength for the ~735 nm wide waveguide portions of the DBR. At the wider sections of the DBR, the first order TE mode can couple with this mode, which is leaky since it cannot propagate through the entirety of the DBR due to the fact that the third order TE mode is not allowed at the narrower sections of the DBR.

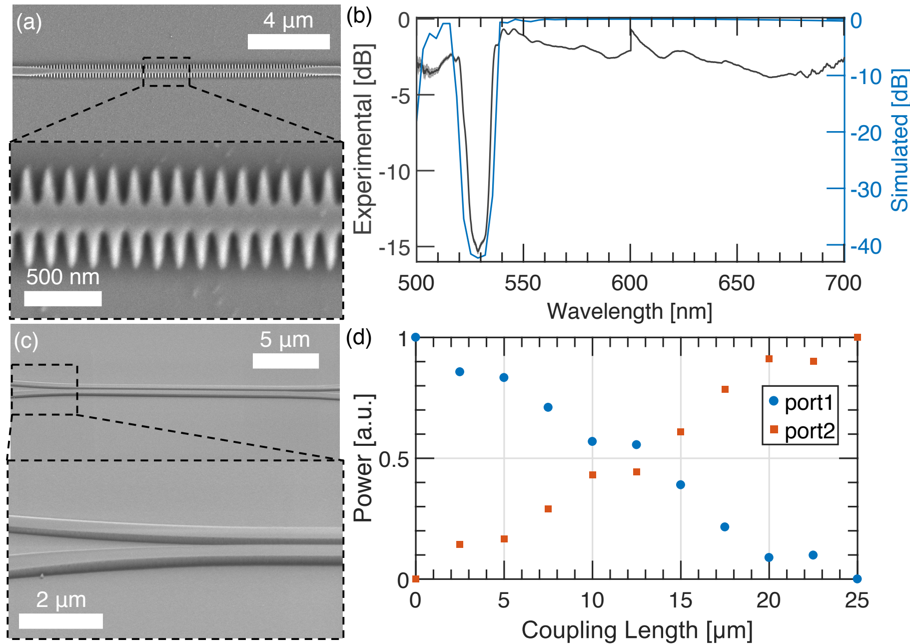

Fig. 5. (a) SEM of the distributed Bragg reflector (DBR) with adiabatic tapering for low insertion loss. Inset shows a zoom-in of the DBR. (b) Simulated and measured transmission vs. wavelength for the DBR. In simulation, we achieve 45 dB extinction for 532 nm green pump light typically used for NV excitation. Experimentally, we achieve >13 dB extinction for 532 nm. (c) SEM of directional couplers with 50/50 splitting ratio at a 50 degrees tilted view. Inset shows a zoom-in of the directional couplers at a 50 degrees tilted view. (d) Measured transmission power at the two output ports of the directional couplers as a function of coupling length in the straight, parallel waveguides region.

4.4. Directional coupler

Figure 5(c) shows a directional coupler with a 50/50 splitting ratio, which is the integrated photonics equivalent of a free space beamsplitter, for the wavelength of 637 nm. The directional coupler is intended to be used with PMMA cladding. Directional couplers coherently couple between adjacent waveguide modes and can be used as a building block for Mach-Zehnder interferometers (MZIs) [35]. Figure 5(d) shows the power at the output two arms of the directional coupler as the length of the straight, parallel waveguides portion of the coupling region (denoted as "Coupling Length") is swept for different devices. The gap between the two straight, parallel waveguides in the coupling region is 200 nm. A coupling length of 14 μm results in a 50/50 splitting ratio. We subtract the power measured at each of the two output ports of the directional coupler by the background noise. Since the power at the output port 2 for a coupling length of 0 μm is at the noise floor of our system, we get that there is zero transmission for port 2. The same can be said about output port 1 for a coupling length of 25 μm.

Theoretically, for a pair of coupled waveguides with the same geometry and dimensions, the fraction of cross-coupled power K is given by the following, where Δn is the effective refractive index difference between the symmetric and antisymmetric supermodes and L is the length of the directional coupler [36]:

$$K = \sin^2\left(\frac{\pi L \Delta n}{\lambda}\right) \tag{5}$$

By using a mode solver to calculate Δn and solving for Eq. (5) to get 50/50 splitting ratio ($K = 0.5$), we get that L should be 23 μm. However, this does not take into account the coupling from one waveguide into the other as the two waveguides are brought to the desired separation of 200 nm in the evanescent coupling region via waveguide bends. In simulating the full directional coupler structure with the evanescent waveguide coupling region and bent region, we find a coupling length of 14 μm necessary for achieving 50/50 splitting, matching well to the experimental result.

5. Discussion and conclusion

The UV propagation loss shown here at 369.5 nm is several tens of orders of magnitude lower than the propagation loss shown by Stegmaier et al. for 400 nm wavelength in an AlN on SiO_2 platform [37]. Furthermore, the crystalline materials in our AlN on sapphire platform allow for refined Raman and other parasitic processes to be localized and minimized [38]. Although the UV single mode propagation loss presented here is higher than that shown in SiN-on-SiO_2 multimode and planar waveguides for wavelength at the lower end of the visible spectrum [39, 40] and silica-on-silicon waveguides in theory for UV and VIS [41,42], SiN-on-SiO_2 and silica-on-silicon platforms are limited to passive components and thermo-optic tuners [43]. Furthermore, silica waveguides are typically a couple of microns in dimension with large bend radii and are not ideal for compact, high-density, large-scale photonic integration. Hence, our AlN on sapphire platform, to date, has the record-low waveguide propagation loss down to UV wavelength for active optical materials with $\chi^{(2)}$ properties and supports chip-scale, compact, CMOS-compatible integration [37, 44]. Nonetheless, we believe that there are many sources of loss that can be eliminated or improved upon. One of the main causes for the propagation loss is interface scattering from the roughness of the AlN waveguide sidewalls from etching. To reduce the propagation loss by a few orders of magnitude, one can engineer the waveguide dimensions such that the optical mode overlaps minimally with the sidewalls so that the light scatters minimally from the waveguide's faces [34]. Furthermore, the current waveguide fabrication is optimized for vertical sidewalls so that the photonic components experimentally match well with the simulated design. As such, the reactive-ion etching necessitates a fast physical etch that causes the sidewalls to be rougher than could be possible with a more chemical etch. Sidewall roughness of less

than 0.1 nm is often the benchmark for achieving interface scattering close to that of the bulk scattering limit of optical materials [45]. It may be possible to further optimize the etching parameters to reduce loss. In addition, there is an inherent roughness of the top surface of the AlN thin film from the unoptimized growth. As AlN grown on top of sapphire is still not at the level of silicon on insulator (SOI) wafers made by Smart-Cut® technology used in conventional integrated photonic platforms [46], we expect there to be room for improvements. Finally, the AlN thin film we use is crystalline in the growth direction and polycrystalline in the in-plane direction. Replacing this material with a completely crystalline AlN thin film grown on top of sapphire should result in a lower dislocation density and defect density, thereby improving the purity of our material so that it would behave closer to what is expected of bulk AlN. Furthermore, the crystallinity of single-crystal AlN grown on top of sapphire has been shown to improve significantly by high temperature annealing [47]. The nonlinear susceptibilities $\chi^{(2)}$ and $\chi^{(3)}$ of AlN are material dependent and approximately independent of the film crystallinity, even when taking into account small variation due to crystal stress/strain during growth. However, the effective nonlinearity experienced for nanocrystalline AlN will have a reduced percentage of that intended crystal axis in the field propagation direction of the waveguide mode, thus reducing the effective nonlinearity when compared to epitaxially grown single crystal AlN. As such, further improvements on the crystallinity of AlN thin film grown on top of sapphire would be beneficial for nonlinear applications as well.

Table 1 shows a comparison of this work with other previously demonstrated UV/VIS photonics platforms that are chip-scale and highly compact, particularly AlN on SiO_2 and SiN on SiO_2. This work shows the highest demonstrated resonator Q factor in the UV, as well as higher VIS resonator Q factor than in previous AlN on SiO_2 work [8]. As the AlN thin film shown in this work is crystalline with fewer absorptive defects and dislocation density than the polycrystalline AlN in previous work, AlN on sapphire can in principle support wavelength into the deep UV; SiN has been shown to have significant optical absorption in wavelengths less than 470 nm and down into the UV range due to silicon incorporation into the layers inherent in the SiN growth [48]. Due to this, even though state-of-the-art SiN on SiO_2 has lower single mode waveguide loss compared to AlN single mode waveguides in the visible wavelength, AlN photonics platforms have the capability to operate in the UV regime. Furthermore, AlN has a high piezoelectric coefficient and moderately high electro-optic coefficient compared to materials used in commercially available phase and amplitude modulators, allowing for active optical components. Finally, AlN's high thermal conductivity κ and small thermo-optic coefficient dn/dT allows devices to be less sensitive to temperature fluctuations, which is important for its many potential applications that require high-precision manipulation, routing, and read-out.

In conclusion, we have demonstrated a PIC platform based on the crystalline, wurtzite AlN on top of a sapphire substrate. Both AlN and sapphire are wide bandgap (6.015 eV [49] and 8.8 eV [50], respectively) and transparent from the UV to the mid-infrared [11, 51, 52]. We observe record-high quality factors exceeding 20,000 down to 369.5 nm, which corresponds to record-low propagation loss at 369.5 nm for active optical materials that have $\chi^{(2)}$ properties. The nonlinear, electro-optic, and piezo-electric properties of AlN make it a promising active material for controlling and connecting atomic and atom-like quantum memories, as well as for other applications such as UV spectroscopy and solar-blind communications.

Optics EXPRESS

Table 1. Comparison of different demonstrated UV/VIS photonics platforms.

	AlN on sapphire (this work)	AlN on SiO_2 [8, 11]	SiN on SiO_2 [53, 54]
Resonator Q factor	Q = 24k (369.5 nm) Q = 140k (638 nm)	Q = 7k (410 nm) [a)] [55] Q = 110k (774 nm) [8]	Q = 4.4k (290 nm) [b)] [56]
Supporting wavelength	UV (~210 nm) to IR [11, 51, 52]	UV (~320 nm) to IR [8]	VIS (~470 nm) to IR [39]
Crystallinity	Crystalline	Polycrystalline (c-axis grown)	Stoichiometric
Active properties	electro-optic: r_{33} = ~1 pm/V piezoelectric: d_{33} = ~5 pm/V [52, 57, 58]		electro-optic: 8.31 fm/V [59]
Single mode WG loss	75 dB/cm (369.5 nm) [c)] 5.3 dB/cm (638 nm) [c)]	650 dB/cm (400 nm) [37] 6.4 dB/cm (774 nm) [c)]	< 1 dB/cm (532 nm) [60] 1.5 dB/cm (850 nm) [61]
Thermal properties (waveguide material)	κ = 285 W/m·K dn/dT = 2.32×10^{-5}/K [11]		κ = 1.4 W/m·K dn/dT = 1.0×10^{-5}/K [62]

[a] AlN disk resonator on Si pedestal
[b] Disk resonator
[c] Loss estimated from resonator Q factor

Funding

Air Force Office of Scientific Research Multidisciplinary University Research Initiative (FA9550-14-1-0052); Air Force Research Laboratory RITA program (FA8750-14-2-0120 and FA8750-16-2-0140); Office of the Director of National Intelligence (ODNI), Intelligence Advanced Research Projects Activity (IARPA), via Raytheon BBN Technologies Corp. Contract number 2017-17063000002.

Acknowledgments

The authors would like to thank Dr. Gabriele Grosso, Professor Tim Schröder, and Benjamin Lienhard for helpful discussions about the optical measurement and characterizations. The authors would also like to thank Professor Tomás Palacios, Professor Parsian Mohseni, and Dr. Noelia Vico Triviño for helpful discussions about the AlN material, particularly regarding growth and optical properties. T.-J. L. acknowledges support from the Department of Defense National Defense Science and Engineering Graduate Fellowship. M. F. would like to acknowledge support of this work from the Office of the Secretary of Defense (OSD) ARAP QSEP program. H. C. was supported in part by a Samsung Scholarship and the Air Force Office of Scientific Research (AFOSR) MURI on Optimal Quantum Measurements and State Verification. S. M. was supported in part by the NSF IQuISE program and the NSF program ACQUIRE: "Scalable Quantum Communications with Error-Corrected Semiconductor Qubits." D. Z. was supported by a National Science Scholarship from A*STAR, Singapore. H. M. was supported in part by a Samsung Scholarship. Any opinions, findings, and conclusions or recommendations expressed in this material are those of the author(s) and do not necessarily reflect the views of the Air Force Research Laboratory nor the official policies, either expressed or implied, of ODNI, IARPA, or the U. S. Government. The U. S. Government is authorized to reproduce and distribute reprints for governmental purposes notwithstanding any copyright annotation therein.